SIMULATION OF A DUAL ARM COMPRESSIVE MULTISPECTRAL IMAGER IN THE VISIBLE AND IR RANGE

YENNI PALOMA VILLA ACUÑA

UNIVERSIDAD INDUSTRIAL DE SANTANDER
FACULTY OF PHYSICAL-MECHANICAL ENGINERRING
SCHOOL OF ELECTRICAL, ELECTRONICS AND TELECOMMUNICATIONS ENGINEERING
BUCARAMANGA
2015

SIMULATION OF A DUAL ARM COMPRESSIVE MULTISPECTRAL IMAGER IN THE VISIBLE AND IR RANGE

YENNI PALOMA VILLA ACUÑA

Thesis submitted in partial fulfillment of the requirements for the degree of:
Bachelor of Science in Electronics Engineering

Director:
HENRY ARGUELLO FUENTES
PhD. Electrical and Computer Engineering

UNIVERSIDAD INDUSTRIAL DE SANTANDER
FACULTY OF PHYSICAL-MECHANICAL ENGINERRING
SCHOOL OF ELECTRICAL, ELECTRONICS AND TELECOMMUNICATIONS ENGINEERING
BUCARAMANGA
2015

A los únicos merecedores de todos mis triunfos,

mis padres.

AGRADECIMIENTOS

Agradecimiento especial a Dios por su infinita generosidad,
al darme el privilegio de pertenecer a tan hermosa familia con tan solidos valores.

A mis padres, por ser el motor y la razón de mi vida.
Gracias por tantos años de sacrificio y esfuerzo desinteresado,
son ustedes la única y más perfecta definición de la palabra AMOR
.
A mi hermanita Mónica por ser mi confidente, el consejo diario que sin pedir obtenía,
me ahorraste mucho tiempo y evitaste muchos pasos con tus enseñanzas, ¡TE ADORO!

A Yasser y Angie, mi mejor compañía en estos cinco años y soporte en días difíciles.
Gracias por su incondicional amistad, ambos excelentes ingenieros, solo puedo augurarles
que ¡el éxito los sorprenderá a donde quiera que vayan!

A mi director Henry Arguello, por la oportunidad de trabajar con él en éste proyecto.
Pero en especial por sus valiosos aportes y paciencia.

A los profesores Daniel Sierra, Jaime Barrero y Julio Gelvez por su excelente labor
docente, su esfuerzo y dedicación les ponen la exigencia que la escuela apremia.
Ojalá todos fueran como ustedes.

Y a todos aquellos que con su presencia y aliento me han acompañado en éste trayecto.

Paloma

CONTENTS

Page.

Introduction.....12

1. Compressive sensing background.....17

1.1 Sparsity.....17

1.2 Incoherence.....18

1.3 CASSI background.....19

2. Dual arm (DA)-cassi system......21

2.1 DA-CASSI mathematical model.....22

2.2 DA-CASSI reconstruction process.....28

3. Coded apertures design, compression ratio and gaussian noise.....30

4. Computer simulations and results.....33

4.1 Power analysis of the sparse representations.....36

4.2 Reconstruction of the spectral images.....37

4.2.1 Optimal parameters analysis.....38

4.2.2 Noise analysis.....43

5. Conclusions.....**46**

6. Future work.....**47**

References.....**48**

Bibliography.....**51**

LIST OF FIGURES

Page.

Figure 1. Light propagation through the CASSI system. 19
Figure 2. DA-CASSI optical architecture. 21
Figure 3. Light propagation through the DA-CASSI system.....24
Figure 4. Single shot sensing matrix **H** example 25
Figure 5. Coded apertures with a transmittance of a) 20%. b) 50% and c) 80%...31
Figure 6. Spectral bands of “Moffet field” data cube 34
Figure 7. Spectral bands of “Salinas” data cube 35
Figure 8. Comparison percentage of energy contained as a function of the number of coefficients.....36
Figure 9. Correlation matrix for (a) Moffet field and (b) Salinas databases. 37
Figure 10. Impact of the transmittance ξ in the PSNR of the reconstructed images as a function of the number of snapshots K.....39
Figure 11. Comparison of the best achieved reconstructed images (ξ=0.4 and ρ=52.73%) between CASSI and DA-CASSI.....41
Figure 12. Spectral signatures of P1 and P2 for ξ=0.4, ρ=52.73%.. 43

LIST OF TABLES

Page.

Table 1. Dual spectra sensors on satellites and aircrafts.....15
Table 2. DA-CASSI model variables 27
Table 3. Averaged PSNR of the reconstructed bands for the optimal transmittance values as a function of K. 40
Tabla 4 Averaged PSNR of the reconstructed bands for ξ=0.4 and ρ=52.73% as a function of the SNR noise.....44

RESUMEN

TÍTULO: SIMULACIÓN DE UN SISTEMA DUAL PARA EL MUESTREO COMPRESIVO DE IMÁGENES MULTIESPECTRALES EN EL ESPECTRO VIISBLE E INFRARRROJO CERCANO[*].

AUTOR: YENNI PALOMA VILLA ACUÑA.[**]

PALABRAS CLAVE: Muestreo Compresivo, Sistema Dual, Infrarrojo, Visible

La espectroscopia de imágenes involucra el muestreo de la información espacial de un objetivo a lo largo de un conjunto de longitudes de onda, en el que se adquiere un cubo de datos de tres dimensiones, dos de ellas espaciales y una espectral. El sistema CASSI es una arquitectura sobresaliente utilizada para adquirir este tipo de imágenes utilizando la teoría del muestreo compresivo para recuperar el cubo de datos a partir de una menor cantidad de medidas que la establecida por el teorema de Shanon-Nyquist. Las imágenes espectrales juegan un papel importante en muchos campos de la ciencia y la tecnología, algunas de sus aplicaciones exigen la adquisición de la imagen en el espectro visible e infrarrojo, con el fin de detectar características no distinguibles a simple vista, presentes en capas inferiores del objetivo donde la luz visible no alcanza a atravesar. Estas aplicaciones requieren de un sistema óptico que cuente con un detector extra que sea sensible al espectro infrarrojo, lo cual aumenta significativamente los costos totales del sistema de adquisición. Este trabajo propone un sistema que reduce dichos costos de implementación adquiriendo simultáneamente la imagen en el espectro visible e infrarrojo. Además evalúa si la calidad de las imágenes reconstruidas es lo suficientemente buena para considerar su implementación óptica. Se realizaron diversas simulaciones para determinar la relación señal a ruido pico (PSNR, por su sigla en inglés) de los cubos de datos reconstruidos, en función de la transmitancia de los códigos de apertura, el ruido Gaussiano aplicado a las mediciones y el número de capturas. Los valores de PSNR obtenidos alcanzan los 33 dB.

[*] Trabajo de grado.

[**] Facultad de Ingenierías Físico-Mecánicas, Escuela de Ingenierías Eléctrica, Electrónica y de telecomunicaciones.Director: Henry Arguello Funtes.

ABSTRACT

TITTLE: SIMULATION OF A DUAL ARM COMPRESSIVE MULTISPECTRAL IMAGER IN THE VISIBLE AND NEAR INFRARED RANGE[*].

AUTHOR: YENNI PALOMA VILLA ACUÑA[**].

KEY-WORDS: SPECTRAL IMAGING, COMPRESSIVE SENSING, DUAL ARM, INFRARED, VISIBLE.

Imaging spectroscopy involves the sensing of the spatial information of a scene across a range of wavelengths, such that a three-dimensional data cube is acquired. The coded aperture snapshot spectral imaging is an outstanding architecture for sensing this kind of images, which effectively applies the compressive sensing theory to reconstruct the data cube from fewer samples than those stated by the Shannon-Nyquist theorem. Spectral images play an important role in science and technology, some of their applications require the image acquisition in both the visible and the infrared ranges in order to detect characteristics not noticeable to the bare eye, which can be perceived in lower layers of the scene where the visible light does not go through. These applications require an optical system with an infrared sensitive extra-detector that significantly increases the cost of the acquisition system. This paper proposes an image acquisition compressive system that reduces the number of optical elements, by jointly and compressively acquiring the images in the visible and infrared spectra and also evaluates whether the quality of the reconstructed images is good enough to consider the optical implementation of the proposed system. Diverse simulations are performed to determine the peak signal to noise ratio (PSNR) of the data cubes as a function of the coded apertures transmittance, the Gaussian noise applied to the measurements and the number of snapshots. The simulations give PSNR values up to 33 dB in the reconstructed images.

[*] Research Project.

[**] Faculty of Physical-Mechanics Engineering. Electrics, Electronics and Telecomunications School. Advisor: Henry Arguello Funtes.

INTRODUCTION

Spectrometers are instruments for measuring the intensity or polarization of electromagnetic waves across a wide range of wavelengths, i.e. their spectral signature. Despite spectrometers give precise spectral information of a specific spatial point, some applications are more interested on scanning the whole scene, making necessary the sensing of all spatial points [1]. These instruments are known as spectral imagers as they acquire both, spatial (x, y) and spectral (λ) information of a scene in a 3D data cube. Depending on the band width and the continuous nature of the recorded bands, these data cubes can be classified as multi or hyperspectral images; while the multispectral images measure the reflected radiation by a surface in large but very separated frequency bands, hyperspectral images are acquired in tens or hundreds of narrow and contiguous bands [2], making possible to build a high-resolution spectral signature for each spatial point of the scene. Therefore, multispectral images are not proper for detecting fine details on the scene surface or classifying objects that present a very little difference in terms of their spectral content [3].

Spectral images play a very important role in various areas of science and technology such as: remote sensing [2], agriculture [4] and quality control [5]. Near infrared (NIR) spectroscopy utilizes the spectral information in the range from 780 to 2500 [ηm] to provide more complex structural information related to the vibration of combination of bonds. Numerous NIR studies demonstrate that it is a non-destructive and rapid technique in the food quality assessment since it reveals information related to the vibrational behavior of molecular bonds and therefore can give details of the molecules varieties present in the food [6]. For this reason, some applications require the image acquisition in the visible (V) and infrared spectrum (IR), in order to detect characteristics not visible to the bare eye, which

can be perceived in lower layers of the scene where the visible radiation does not go through [7]. Thus, not only visible but also infrared data is of high interest for these applications. However, the development of this work is mainly concerned with the spectral imagers developed for remote sensing, since this is a technology that focuses on providing quantifiable information from the visible to the thermal infrared range of a remote environment to enhance our understanding of physical phenomena occurring there. E.g., for agriculture, it is the visible - infrared range of the spectrum that potentially allows the identification and classification of vegetation [8] as well as weather forecasting, water color mapping to identify the presence of microorganisms and pollutants, stress analysis of in-field crops and so on [3].

There are two main classes of spectral imagers, either spectrally or spatially discriminatory, depending on what dimension the scanning has to be made across the remaining 2D to complete the 3D data cube. An example of a spectrally discriminatory instrument is a 2D spatial camera based on band pass filters [9]; this architecture is used to scan all spectral channels by sequentially tuning the bandwidth in steps, requiring the scene to be completely static during each spectral acquisition in order to acquire the same spatial matrix for every frequency range. Meanwhile, the spatial scanning approach is characteristic of push broom [1] and whiskbroom [10] architectures, depending on whether it is captured a single pixel at a time or a spatial line of the scene respectively.

The main drawback of these two classes is that the number of zones to be scanned grows proportionally to the desired spatial or spectral resolution. Conversely, in the recently emerged compressive spectral imaging (CSI) approach, the detector measures 2D random coded compressed projections. Here, the number of required measurements for the reconstruction is far less than in the linear scanning case. CSI relies on compressive sensing (CS) principles: sparsity and incoherence [11-12]. The sparsity of an image refers to the property of natural

signals of having a more concise representation when expressed in a convenient basis whilst incoherence relates to the sensing modality between the representation and sensing basis of the imaging system. In summary, these two properties become the heart of CSI, since an appropriate design of both, the measurement matrix $\mathbf{\Phi}$ and the sparsifying basis $\mathbf{\Psi}$ are essential to achieve maximum CS efficiency [1].

The coded aperture snapshot spectral imager (CASSI) is an architecture that effectively applies the CS theory to improve the sensing speed and reduce the large amount of data to far fewer measurements than that established by Nyquist/Shannon theorem, making possible to acquire the entire data cube with just a few focal plane array (FPA) measurements [1,12]. The theoretical background of CASSI is applicable for any region of the electromagnetic spectrum determined by the spectral sensitivity of the optical elements. Therefore, as there is no technology developed in sensitive sensors to such a wide frequency ranges, to capture images in both visible and infrared it is necessary to use an architecture that separately acquires the information into the appropriate detector. It could be realized by using separately two CASSI systems, resulting in an expensive system to implement; the dual arm (DA)-CASSI system presented in this paper, rises as an alternative to reduce the implementation costs of that solution, by jointly capturing the spectral information of both ranges.

It is important to take into account that regardless of the class, all sensing systems must reside on a stable platform away from the scene to be scanned. In remote sensing these systems are commonly carried in aerial vehicles like choppers, aircrafts and unmanned aerial vehicles (UAV) or on spacecraft platforms outside of the earth's atmosphere such as space-shuttle and satellites. A classified per flight mode list containing the class and some operating parameters of the most popular existing platforms, that must use dual sensors due to the wide range of frequencies they acquire, are exposed in Table 1. As it can be noticed there, there are no

compressive spectral imagers implemented to simultaneously acquire images in the visible and infrared range.

This document is organized as follows: first, the background about CS theory and the multi-shot CASSI system are exposed, as well as a brief explanation about the system parallelization for separately acquiring the image in each spectral range. Then, the optical-mathematical model for the DA-CASSI system is presented. Finally, simulations and results to quantitatively compare the performance of the proposed system against two separate CASSI systems are presented.

Table 1. Dual Spectra Sensors on Satellites and Aircrafts

TYPE OF SENSORS	PRODUCER	SPATIAL RES. [M]	SPECTRAL RANGE [μm] (BANDS)	CLASS
Remote sensing sensors on spacecrafts				
FTHSI on MightySat II	Air Force Research	30	0.47-1.05 (256)	Pushbroom
Hyperion on EO-1	NASA Guddard Space Flight Center	30	0.40-2.50 (242)	Pushbroom
AVHRR/3 (Advanced Very High Resolution Radiometer)	NOAA Satellite information system	1090	0.58-12.5 (6)	Whiskbroom
ASTER	NASA Jet Propulsion Lab.	15 to 90	0.5-11.65 (15)	Pushbroom
Remote sensing sensors on aircrafts				
AVIRIS (Airborne Visible Infrared Imaging Spectrometer)	NASA Jet Propulsion Lab.	20	0.40-2.50 (224)	Whiskbroom
HYDICE (Hyperspectral Digital Imagery Collection Experiment)	Naval Research Lab.	1 to 4	0.40-2.50 (210)	Pushbroom

TYPE OF SENSORS	PRODUCER	SPATIAL RES. [M]	SPECTRAL RANGE [μm] (BANDS)	CLASS
PROBE-1	Earth Search Sciences Inc.	5	0.40-2.45 (128)	Pushbroom
CASI (Compact Airborne Spectrographic Imager)	ITRES Research limited	2	0.4-1.05 (Over 228)	Pushbroom
HyMap	Integrated Spectronics	2 to 10	0.4-12.00 (100 to 200)	Whiskbroom
EPS-H (Environmental Protection System)	GERIS Corporation (Geophysical & Environmental Research Imaging Spectrometer)	n/a	0.43-12.50 (152)	Whiskbroom
DAIS 7915 (Digital Airborne Imaging Spectrometer)	GERIS Corporation	n/a	0.40-12.60 (79)	Whiskbroom
DAIS 21115 (Digital Airborne Imaging Spectrometer)	GERIS Corporation	n/a	0.40-12.00 (211)	Whiskbroom
AISA DUAL (Airborne Imaging Spectrometer)	Spectral Imaging Specim	5	0.40-2.50 (up to 500)	Pushbroom

Source: Adapted from [3,10, 13, and 14].

1. COMPRESSIVE SENSING BACKGROUND

CS effectively reduces the acquisition time and the number of acquired measurements by simultaneously sensing and compressing the data, instead of sensing directly the signal and then compressing it, in the post processing stage. In this way, the cost of the system is reduced as well as its storage requirements. To do so, CS relies on two principles: sparsity and incoherence.

1.1 SPARSITY

CS exploits the fact that many natural signals have a more compact representation in a convenient basis [11]. More formally, let $\mathbf{f} \in \mathbb{R}^N$ be the signal of interest and, $\boldsymbol{\theta}$ be the representation of $\mathbf{f}$ in the basis $\boldsymbol{\Psi}$, such that $\mathbf{f} = \boldsymbol{\Psi}\boldsymbol{\theta}$. Then, we say that $\mathbf{f}$ is $S-$sparse if the orthonormal basis $\boldsymbol{\Psi} \in \mathbb{R}^{NxN}$ sparsifies $\mathbf{f}$, when $\boldsymbol{\theta} = \boldsymbol{\Psi}^{\mathrm{T}}\mathbf{f}$ has only $S \ll N$ non-zero entries, where $\boldsymbol{\Psi}^{\mathrm{T}}$ is the transpose matrix of $\boldsymbol{\Psi}$. Otherwise, we say that $\boldsymbol{\Psi}$ compresses $\mathbf{f}$, if the sorted by magnitude entries of $\boldsymbol{\theta}$ decay according to $|\boldsymbol{\theta}(i)| < Ci^{-1/p}$ for any $p \leq 1$, and $C < \infty$. Then, it is said that $\boldsymbol{\theta}$ is $S-$compressible in $\boldsymbol{\Psi}$, by retaining the S largest coefficients by magnitude and setting the rest to zero [15].

A sparse representation means that the number of non-zero coefficients in $\boldsymbol{\theta}$ is S with $S \ll N$. A compressible representation, on the other hand, means that the coefficient's magnitudes in a given basis, when sorted, have fast power-law decay. Strictly talking, most signals of interest are not exactly sparse but approximately sparse or compressible in a convenient basis, and the selection of the basis in which the signal is compressible is crucial to obtain better reconstruction results.

Previous work has proven that the Kronecker product sparsifying basis gives the sparsest spectral images since for multidimensional signals, such matrices act as sparsifying bases that jointly model the structure present in every signal dimension [15]. Suppose $\mathbf{F} \in \mathbb{R}^{MxNxL}$ is a hyperspectral signal, or its vector representation $\mathbf{f} \in \mathbb{R}^{MNL}$ is S-sparse on some basis $\mathbf{\Psi}_{3D}$, then $\mathbf{f}$ can be expressed as a linear combination of S vectors of $\mathbf{\Psi}_{3D}$ as follows

$$\mathbf{f} = \mathbf{\Psi}_{3\mathrm{D}}\boldsymbol{\theta}, \tag{1.1}$$

where $S \ll MNL$ and $\mathbf{\Psi}_{3\mathrm{D}}$ is the Kronecker product of three bases $\mathbf{\Psi}_1 \otimes \mathbf{\Psi}_2 \otimes \mathbf{\Psi}_3$. Usually, $\mathbf{\Psi}_{3D}$ is set to be the Kronecker product of the 2D-Wavelet symmlet 8 basis (used for the spatial dimensions) and the 1D-DCT basis (for the spectral) such that $\mathbf{\Psi}_{3\mathrm{D}} = \mathbf{\Psi}_{\mathrm{W2D}} \otimes \mathbf{\Psi}_{\mathrm{DCT}}$ [16,17].

1.2 INCOHERENCE

The spectral images compressibility also depends on how similar the sparsifying and the sensing bases are, which can be quantified by their mutual coherence. Mathematically, the mutual coherence of two orthonormal bases $\mathbf{\Phi} \in \mathbb{R}^{N\times N}$ and $\mathbf{\Psi} \in \mathbb{R}^{N\times N}$ is defined as the maximum absolute value for the inner product between elements of the two bases, as follows

$$\mu(\mathbf{\Phi}, \mathbf{\Psi}) = \sqrt{N} \cdot \max_{1\le k,j\le N} \left| < \mathbf{\Phi}_k, \mathbf{\Psi}_j > \right|. \tag{1.2}$$

In this case, $\mathbf{\Psi}$ and $\mathbf{\Phi}$ are the sparsifying and sensing bases respectively, $\mathbf{\Psi}_j(t)$ is the j^{th} column of the representation basis matrix and, $\mathbf{\Phi}_k(t)$ is the k^{th} row of the sensing matrix. From Eq. (1.2), if $\mathbf{\Psi}$ and $\mathbf{\Phi}$ contain correlated elements, the

coherence is large. Otherwise, it is small. Thus, a lower value of μ indicates lower coherence or better incoherence between the measurement and the sparsifying bases. For CS, smaller mutual coherence values demand fewer measurements for achieving certain accuracy in the reconstructed signals. For this reason, as random matrices are largely incoherent with any fixed basis $\mathbf{\Psi}$, the selection of an orthobasis $\mathbf{\Phi}$ uniformly at random promotes CS efficiency [11].

1.3 CASSI Background

The CASSI system depicted in Fig. 1 is composed by six optical elements: an objective lens that focuses the scene $\mathbf{F}$ onto the fixed coded aperture (CA); a set of coded apertures $\mathbf{T}^{\ell}$ to perform the coding, with $\ell = \{1, \dots, K\}$ and K the total number of shots; a band pass filter that limits the incoming source; a dispersive element S_k to shift horizontally the coded field; an imaging lens to relay the coded filtered and spectrally sheared field onto the FPA image plane, where it is finally integrated over the spectral sensitivity $\Delta\Lambda$.

Figure 1. Light propagation through the CASSI system.

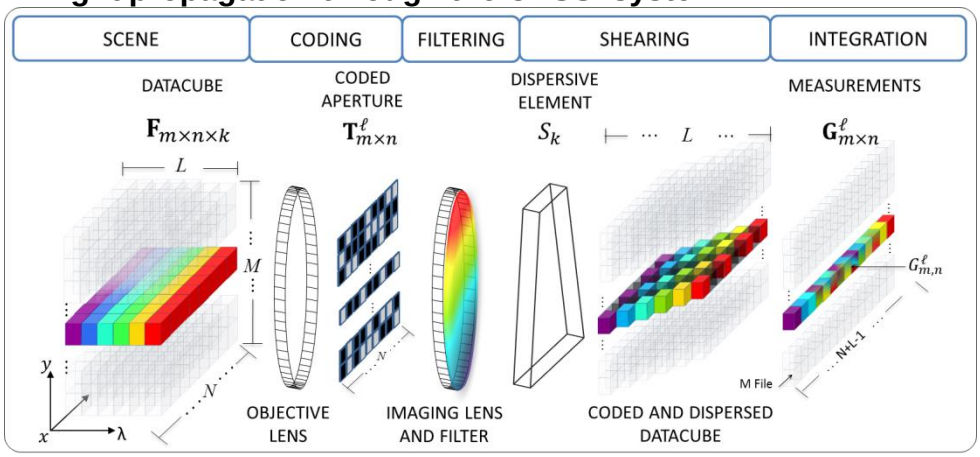

The input signal $\mathbf{F}$ is coded by the CA $\mathbf{T}^{\ell}$, filtered and then dispersed by the prism S_K. Finally, the coded and dispersed signal is integrated on the FPA detector. Source: Adapted from [17].

Assuming idealities in all optical elements, including linear dispersion by the dispersive element, the ℓ^{th} FPA measurement in the (m,n) pixel, $G^{\ell}_{m,n}$, can be expressed as

$$G^{\ell}_{m,n} = \sum_{k=0}^{L-1} F_{m,n-k,k}\, T^{\ell}_{m,n-k} + \omega_{m,n}\,, \tag{1.3}$$

where *L* is the total number of resolvable bands and ω is the noise of the system.

Particularly, denote $\mathbf{g}^{\ell}$ the vector representation of the ℓ^{th} FPA measurements $\mathbf{G}^{\ell}$, which is written in matrix form as $\mathbf{g}^{\ell} = \mathbf{H}^{\ell}\mathbf{f}$, where $\mathbf{H}^{\ell}$ is the transfer function that accounts for the effects of the dispersive element and the ℓ^{th} CA; then the set of *K* FPA measurements can be assembled as $\mathbf{g} = [(\mathbf{g}^{0})^{\mathrm{T}}, \ldots, \left(\mathbf{g}^{\ell}\right)^{\mathrm{T}}, \ldots, (\mathbf{g}^{K-1})^{\mathrm{T}}]^{\mathrm{T}}$, which in turn can be expressed as

$$\mathbf{g} = \mathbf{H}\mathbf{f} + \boldsymbol{\omega}, \tag{1.4}$$

where $\mathbf{H} = [(\mathbf{H}^{0})^{\mathrm{T}}, \ldots, \left(\mathbf{H}^{\ell}\right)^{\mathrm{T}}, \ldots (\mathbf{H}^{K-1})^{\mathrm{T}}]^{\mathrm{T}}$ is the vertical concatenation of the $\mathbf{H}^{\ell}$ matrices.

The principles of CASSI described above are general and applicable to imaging in any region of the electromagnetic spectrum determined by the spectral sensitivity of all the optical elements. To acquire the spectral information of a scene in both visible and IR range, it is possible to realize by using two CASSI systems separately, so that each one acquires the image in a different spectral range. However, in order to reduce the implementation costs, an architecture that jointly senses the scene in both ranges and also gives the information separated on the correspondent detector is proposed in the following section.

2. DUAL ARM (DA)-CASSI SYSTEM.

Figure 2 depicts the DA-CASSI architecture. It is composed by two arms corresponding to the visible and IR paths. When the impinging light source focused by the objective is coded by the DMD, the coded field is divided and addressed by the beam splitter towards each path. Both arms are composed by a band pass filter that band limits the incoming fields; a dispersive element (usually a prism), which horizontally shears the filtered and coded fields; and, the appropriate FPA detector, where the resulting spectral densities are finally integrated.

Figure 2. DA-CASSI optical architecture.

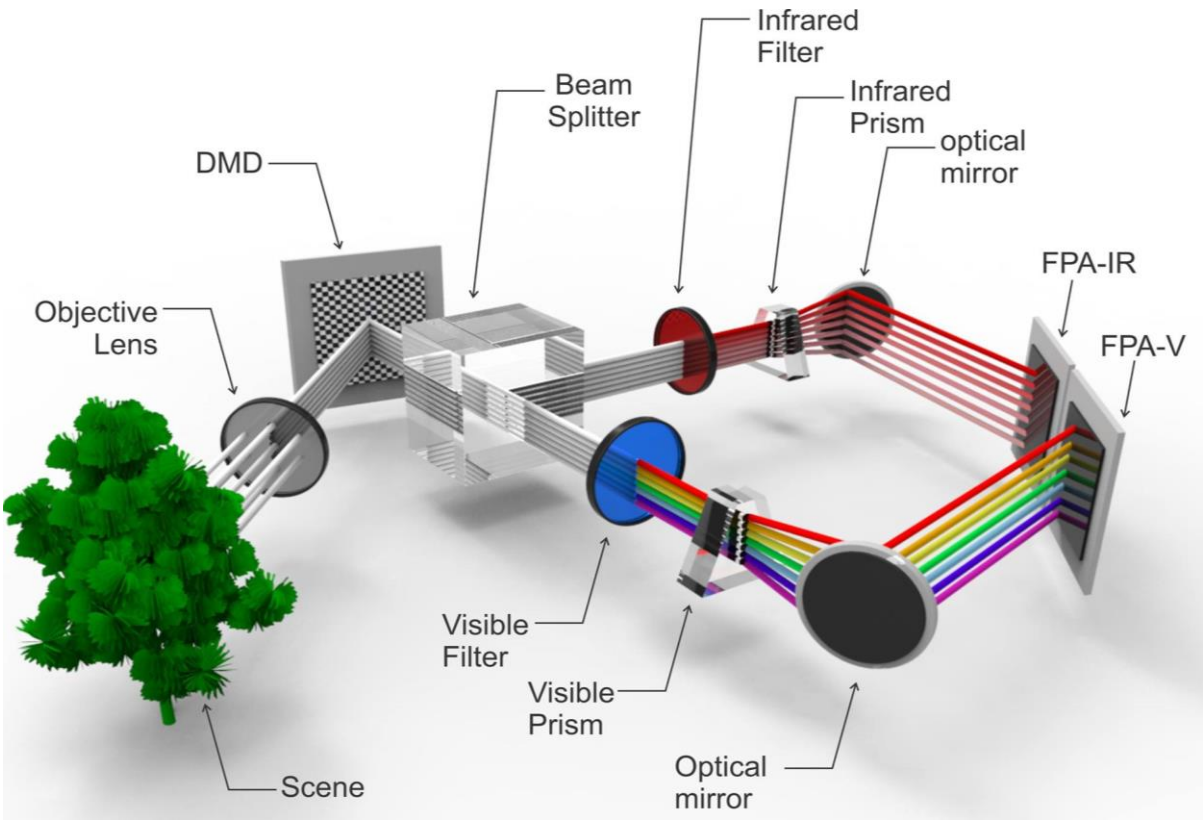

Notice that the two arms of the DA-CASSI share the coding element.

2.1 DA-CASSI MATHEMATICAL MODEL

The light propagation in the optical system begins when the reflected light source is focused by the objective lens into the CA, where the coding is realized by applying $T(x,y)$ to the spatio-spectral density source $f_o(x,y,\lambda)$, yielding to $f_1(x,y,\lambda)$

$$f_1(x,y,\lambda) = T(x,y) f_o(x,y,\lambda), \tag{2.1}$$

where (x,y) are the spatial coordinates and λ is the wavelength of the impinging light. The spectral density $f_1(x,y,\lambda)$ power is equally divided by the beam splitter and sent to the filter of the respective arm. In each path only the wavelengths belonging to that spectral range will pass to the corresponding prism where, they consequently will be dispersed, resulting in the coded fields

$$\begin{aligned} f_{2\mathrm{V}}(x,y,\lambda) &= \iint f_{1\mathrm{V}}(x,y,\lambda) h_{\mathrm{V}}(x' - x - S_{\mathrm{V}}(\lambda), y' - y) dx' dy' , \\ f_{2\mathrm{IR}}(x,y,\lambda) &= \iint f_{1\mathrm{IR}}(x,y,\lambda) h_{\mathrm{IR}}(x' - x - S_{\mathrm{IR}}(\lambda), y' - y) dx' dy', \end{aligned} \tag{2.2}$$

where $\mathrm{h_V}$ and $\mathrm{h_{IR}}$ are the optical impulse responses of the visible and infrared systems respectively, $S_{\mathrm{V}}(\lambda)$ and $S_{\mathrm{IR}}(\lambda)$ are the dispersion functions induced by the prisms corresponding to each spectral range and, the primed variables refer to the spatial location before the CA and the non-primed in the FPA. Finally, $f_{1\mathrm{V}}(x,y,\lambda)$ and $f_{1\mathrm{IR}}(x,y,\lambda)$ are the filtered versions of $f_1(x,y,\lambda)$ in the visible and IR respectively.

Every coded and dispersed field is focused by an imaging lens into the respective FPA where they are integrated over the detector's spectral range sensitivity.

$$g_{\mathrm{V}}(x,y) = \int_{\lambda_o}^{\lambda_{\mathrm{V}}} f_{2\mathrm{V}}(x,y,\lambda)d\lambda, \tag{2.3}$$

$$g_{\mathrm{IR}}(x,y) = \int_{\lambda_{\mathrm{V}}}^{\lambda_{\mathrm{IR}}} f_{2\mathrm{IR}}(x,y,\lambda)d\lambda$$

where the primed variables refer to the spatial location before the CA and the non-primed in the FPA.

Assuming that (i) the PSF h_V and h_{IR} are shift invariant; (ii) there is one-to-one match between coded aperture features and the pixels of the detectors and, (iii) supposing idealities in the optical elements, including linear dispersion by the dispersive element, the measurements at the detectors can be expressed as

$$g_{\mathrm{V}}(x,y) = \int_{\lambda_o}^{\lambda_{\mathrm{V}}} f_o(x - S_{\mathrm{V}}(\lambda), y, \lambda)T(x - S_{\mathrm{V}}(\lambda), y)d\lambda, \tag{2.4}$$

$$g_{\mathrm{IR}}(x,y) = \int_{\lambda_{\mathrm{V}}}^{\lambda_{\mathrm{IR}}} f_o(x - S_{\mathrm{IR}}(\lambda), y, \lambda)T(x - S_{\mathrm{IR}}(\lambda), y)d\lambda.$$

For analysis and computational purposes, the underlying analog phenomenon is discretized such that the spatio-spectral signal $f_o(x,y,\lambda)$ is defined as $\mathbf{F}_{m,n,k}$ and its vector representation is assembled as $\mathbf{f} = [\mathbf{f}_{\mathrm{V}};\ \mathbf{f}_{\mathrm{IR}}]$, where (n,m) indexes the spatial axes (x,y) and k the spectral axis λ; the discretized coded aperture is represented by $\mathbf{T}$. Assuming that the visible filter limits the spectral components between $\{\lambda_0 - \lambda_{\mathrm{V}}\}$ and the infrared between $\{\lambda_{\mathrm{V}} - \lambda_{\mathrm{IR}}\}$, the total number of resolvable bands L is limited by $L_{\mathrm{V}} = \frac{\lambda_{\mathrm{V}} - \lambda_{\mathrm{o}}}{N_{\mathrm{V}}}$ and $L_{\mathrm{IR}} = \frac{\lambda_{\mathrm{IR}} - \lambda_{\mathrm{V}}}{N_{\mathrm{IR}}}$, where the spectral resolution is given by N_{V} and N_{IR}. Figure 3 depicts the discretized model of the light propagation through the DA-CASSI system.

Figure 3. Light propagation through the DA-CASSI system.

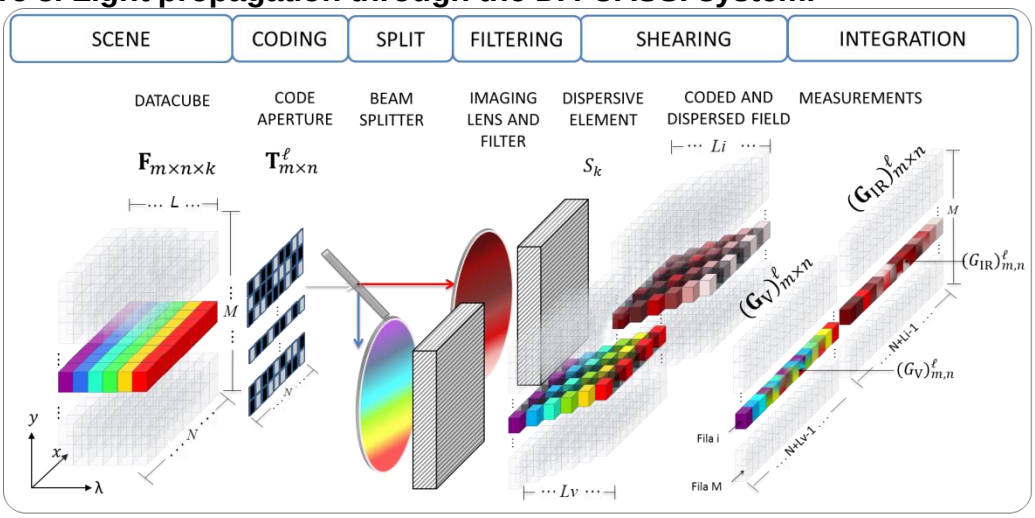

The input signal $\mathbf{F}$ is coded by the CA $\mathbf{T}$; the resulting field power is equally divided by the beam splitter and sent to both arms, where will be filtered and then dispersed by the prism S_{k}. Finally, each coded and dispersed field is integrated into the respective detector.

According to Fig. 3, the discretized output in each detector is modeled as the independent sum of the underlying spectral voxel slices modulated by the same coded aperture $\mathbf{T}$ and dispersed by the corresponding prism. More strictly, the two FPA measurements in m, n for each detector can be expressed as

$$(G_V)_{m,n} = \sum_{k=0}^{L_V-1} (F_V)_{m,n-k,k}\, T_{m,n-k} + (\omega)_{m,n}, \tag{2.5}$$

$$(G_{IR})_{m,n} = \sum_{k=L_V}^{L_{IR}-1} (F_{IR})_{m,n-k,k}\, T_{m,n-k} + (\omega)_{m,n}.$$

In matrix form, eq. (2.5) can be expressed as in eq. (1.4); however, the structure of the sensing matrix is represented as a diagonal matrix where the first sub matrix corresponds to the visible spectrum $\mathbf{H}_{\mathrm{V}}$ and the second for the infrared $\mathbf{H}_{\mathrm{IR}}$, as follows

$$\overbrace{\begin{bmatrix}\mathbf{g}_{\mathrm{V}}\\ \mathbf{g}_{\mathrm{IR}}\end{bmatrix}}^{\mathbf{g}} = \overbrace{\begin{bmatrix}\mathbf{H}_{\mathrm{V}} & \mathbf{0}\\ \mathbf{0} & \mathbf{H}_{\mathrm{IR}}\end{bmatrix}}^{\mathbf{H}} \overbrace{\begin{bmatrix}\mathbf{f}_{\mathrm{V}}\\ \mathbf{f}_{\mathrm{IR}}\end{bmatrix}}^{\mathbf{f}} + \boldsymbol{\omega} \tag{2.6}$$

An example of the sensing matrix $\mathbf{H}$ is illustrated in Fig. 4. This matrix has a diagonal pattern where the circled diagonal vectors repeating horizontally correspond to the distribution of the coded aperture used for both: the visible (top left) and infrared (bottom right) ranges.

Figure 4. Single shot sensing matrix H example for $M = 4, N = 8$, $L_V = 3$ and $L_{IR} = 2$.

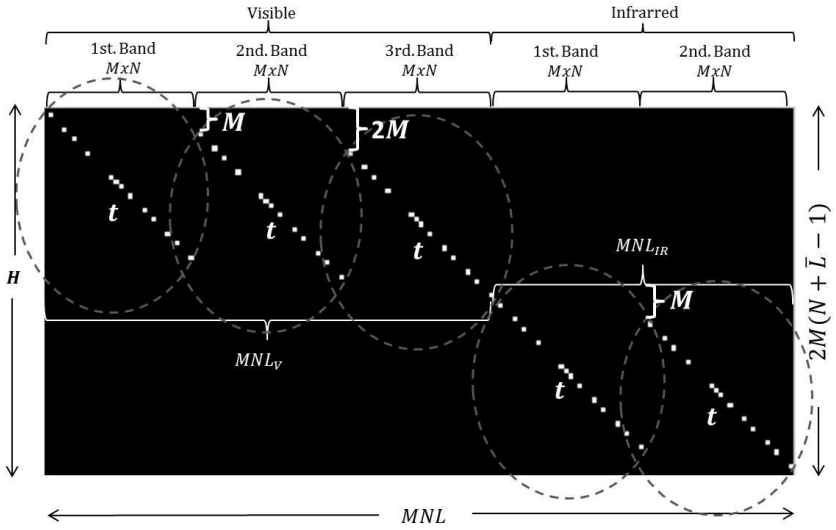

Black squares represent zero-valued elements (blocking light) and the white squares represent one value elements. Notice that the coded aperture $\mathbf{t}$, is the same for the visible and infrared range.

In order to increase the number of compressive measurements when spectrally rich or very detailed spatial scenes are sensed, the multi-shot DA-CASSI allows the acquisition of multiple FPA measurements [16], each using a different CA $\mathbf{T}^{\ell}$ during the integration time of the detector. This can be accomplished in two different ways: by moving a printed thin-film-based CA [18] back and forth using a

high precision piezoelectric device to accurately perform the nanoposition realignment procedure (which significantly increases the system costs), or by using a DMD-based CA [19] that takes advantage of its tilting capabilities to address or deflect the impinging source light to the objective without requiring realignment. Therefore, the DMD-based CA becomes the best practical implementation since it offers a more robust, accurate and reliable multi-shot modulation system at a reduced cost [17].

Figure 7. Multi-shot H matrix example for $K = 2, M = 4, N = 8, L_{\mathrm{V}} = 3$ and $L_{\mathrm{IR}} = 2$.

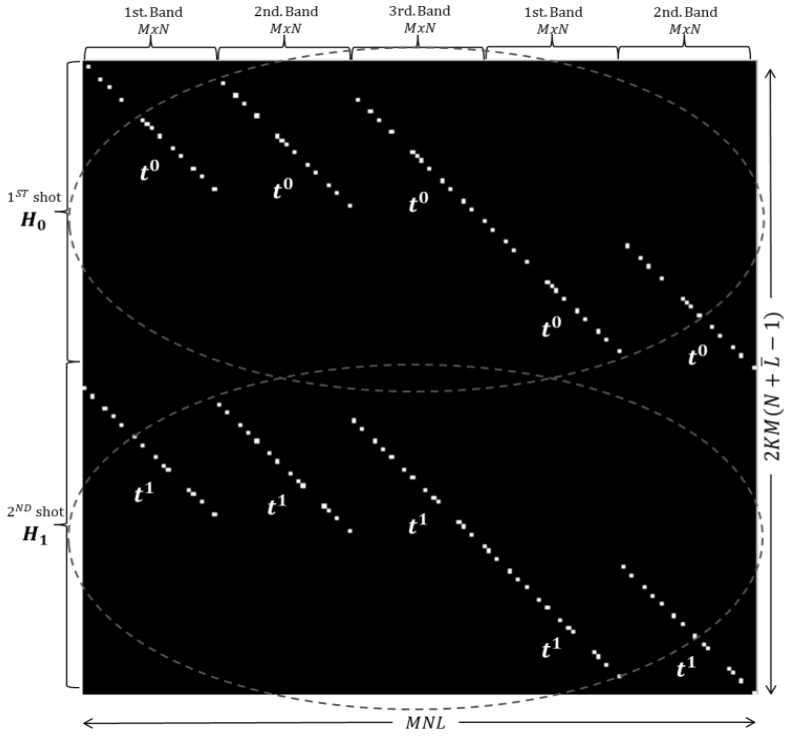

Each circle pattern corresponds to every snapshot taken. Notice that $\mathbf{t}^0$ and $\mathbf{t}^1$ are the vector representations of the code apertures $\mathbf{T}^0$ and $\mathbf{T}^1$ respectively.

The $\mathbf{H}$ matrix for the multi-shot DA-CASSI system can also be expressed as in the conventional CASSI, eq. (1.4), since the modification is implicit for every $\mathbf{H}^{\ell} = [\,{\mathbf{H}_{\mathrm{V}}}^{\ell}\ \mathbf{0}; \mathbf{0}\ {\mathbf{H}_{\mathrm{IR}}}^{\ell}]$. Figure 7 shows an example of a multi-shot $\mathbf{H} =$

$[(\mathbf{H}^0)^{\mathrm{T}} \ldots \left(\mathbf{H}^{\ell}\right)^{\mathrm{T}^{\ell}} \ldots (\mathbf{H}^{\mathrm{K}})^{\mathrm{T}}]$ matrix for *M=4, N=8, K=2* and *L=5*. There, three bands for the visible and two for the infrared range are used. The upper half of this matrix corresponds to the first shot and the lower half matrix accounts for the second one.

Finally, the multi-shot vector of measurements is given by the expression

$$\begin{bmatrix} \mathbf{g}^0 \\ \vdots \\ \mathbf{g}^{\ell} \\ \vdots \\ \mathbf{g}^{\mathrm{K}-1} \end{bmatrix} = \begin{bmatrix} \mathbf{H}^0 \\ \vdots \\ \mathbf{H}^{\ell} \\ \vdots \\ \mathbf{H}^{\mathrm{K}-1} \end{bmatrix} \mathbf{f} + \boldsymbol{\omega}, \tag{2.7}$$

It can be noticed that the $\mathbf{H}$ matrix in eq. (2.7) is sparse and highly structured. Each row contains at most $L_{\mathrm{V}} + L_{\mathrm{IR}}$ non-zero elements and each column contains up to K non-zero elements.

The non-linear dispersion curve of the prisms and other elements such as the imaging or objective lenses, the spectral response of the camera and the coded apertures might be considered ideal mathematically, as long as a prior calibration process is conducted in order to partially mitigate all the deviations from the ideal characteristics assumed.

As shown in Fig. 3, the source light splits after the modulation done by the DMD. For this reason, the DA-CASSI does not require an objective lens and a DMD as two CASSI systems used simultaneously in parallel for the same purpose, which significantly reduces the total costs of the proposed system. Notice that the $\mathbf{f}_{\mathrm{V}}$ and $\mathbf{f}_{\mathrm{IR}}$ images are implicitly aligned in the DA-CASSI, whereas the separate CASSI systems need to be aligned to acquire the same spatial matrix. A summary of the variables employed in the DA-CASSI model is shown in Table 2.

Table 2. DA-CASSI model variables

Description	Name	Size
Number of visible bands	L_{V}	
Number of IR bands	L_{IR}	
Total number of bands	$L = L_{\mathrm{V}} + L_{\mathrm{IR}}$	
Spatial dimensions of **F**	$M \times N$	
Number of shots	K	
Data cube	$\mathbf{F}$	$M \times N \times L$
Vectorized form of **F**	$\mathbf{f}$	MNL
Coded aperture of the ℓ^{th}shot	$\mathbf{T}^{\ell}$	$M \times N$
Vectorized form of $\mathbf{T}^{\ell}$	$\mathbf{t}^{\ell}$	MN
CASSI output of the ℓ^{th} shot	$\boldsymbol{G}^{\ell}$	$M \times 2(N + \overline{L} - 1)$
Vectorized form of G^{ℓ}	$\mathbf{g}^{\ell}$	$2M(N + \overline{L} - 1)$
Vectorized form for *K* CASSI outputs	$\mathbf{g}$	$2KM\left(N + \overline{L} - 1\right)$
CASSI matrix for the ℓ^{th}shot	$\mathbf{H}^{\ell}$	$2M\left(N + \overline{L} - 1\right) \times MNL$
CASSI matrix for *K* shots	$\mathbf{H}$	$2KM\left(N + \overline{L} - 1\right) \times MNL$

2.2 DA-CASSI RECONSTRUCTION PROCESS

As the number of voxels (columns of $\mathbf{H}$) is greater than the number of detector pixels (rows of $\mathbf{H}$) obtained, the system of linear equations represented by $\mathbf{H}$ becomes under-determined or ill-conditioned, hence direct inversion of the transfer function $\mathbf{H}^{-1}$ is unfeasible. However, several numerical algorithms have been designed to solve this kind of convex unconstrained optimization problems. The gradient projection for the sparse reconstruction (GPSR) is one of them, and it is employed to obtain an approximation $\hat{\mathbf{f}}$ of the original data cube $\mathbf{f}$, providing a good trade-off between computational complexity and reconstruction quality. The complexity per GPSR iteration is better explained in [20].

The set of measurements acquired by the FPA $\mathbf{g}$ is used as an input to the GPSR algorithm and the reconstruction is attained by solving the optimization problem

$$\hat{\mathbf{f}} = \boldsymbol{\Psi}^{\mathrm{T}} \left(\underset{\boldsymbol{\theta}}{\operatorname{argmin}} \|\mathbf{H}\boldsymbol{\Psi}\boldsymbol{\theta} - \mathbf{g}\|_2^2 + \tau \|\boldsymbol{\theta}\|_1 \right), \tag{2.8}$$

where τ is a regularization constant, $\mathbf{H}$ is the sensing matrix in eq. (2.6), $\boldsymbol{\theta}$ is a sparse representation of $\mathbf{f}$ on the basis $\boldsymbol{\Psi}$ and the ℓ_1 minimization norm turns small components of $\boldsymbol{\theta}$ to zero and helps to boost sparse solutions. As the GPSR finds a sparse representation of the original data cube in the given basis $\boldsymbol{\Psi}$, to obtain $\hat{\mathbf{f}}$ from the coefficients given by the GPSR, these must be returned to its original domain by applying $\boldsymbol{\Psi}^{\mathbf{T}}$.

Notice that the DA-CASSI reconstruction process uses a greater number of measurements $2KM(N + \bar{L} - 1)$ per iteration to recover $\mathbf{f}$, compared with the parallelized CASSI systems where only $KM(N + L_{\mathrm{V}} - 1)$ or $KM(N + L_{\mathrm{IR}} - 1)$ measurements are employed for separately obtaining $\mathbf{f}_{\mathrm{V}}$ and $\mathbf{f}_{\mathrm{IR}}$ respectively.

3. CODED APERTURES DESIGN, COMPRESSION RATIO AND GAUSSIAN NOISE

The coded aperture design used to modulate the source light plays an important role in the reconstructed signal quality since this set up the spatial modulation. Traditionally, the coded apertures employed in CASSI system include Boolean [16, 18], Bernoulli [17] and gray scaled [21] codes designed randomly [16, 17, 18] or following a Hadamard structure [16, 21]. However, recent work developed in order to enrich coding strategies, proposed the use of colored coded apertures, replacing the block-unblock photomasks by patterned optical filter arrays, as a combination of low-pass, high-pass and band-pass filters so that every pixel from the coded aperture permits to pass just a desired set of wavelengths, allowing the modulation of the scene not only spatially but spectrally as well [17]. In the development of this work, Boolean random coded apertures were used, so that every pixel of the coded aperture, $\mathrm{T}_{\mathrm{m,n}}^{\ell} \in \{0,1\}$, with $\mathrm{T}_{\mathrm{m,n}}^{\ell} = 1$ representing a transmissive code element and $\mathrm{T}_{\mathrm{m,n}}^{\ell} = 0$ a blocking code element. The transmittance ξ of the coded aperture is defined as

$$\xi = \sum_{m=0}^{M-1} \sum_{n=0}^{N-1} \frac{T_{m,n}}{MN}, \tag{3.1}$$

where MN represents the size of the coded aperture. Figure 5 represents the transmittance concept; the pattern in Fig. 5a is blocking a greater number of pixels (a smaller transmittance) than that in Fig. 5c.

Figure 5. Coded apertures of 9x8 pixels with a transmittance of a) 20%. b) 50% and c) 80%.

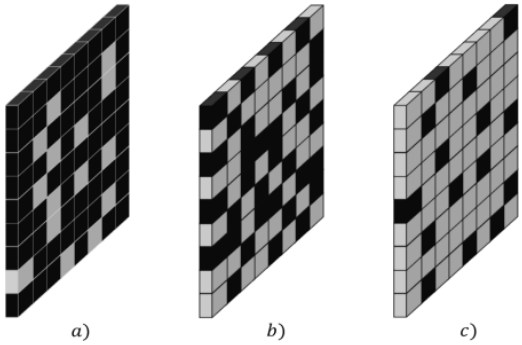

The block squares represent blocking elements whilst white squares permit the light to go through.

In addition to the transmittance, another important variable to analyze is the number of captured snapshots K [3-5]. The compression ratio is the relation between the number of measurements acquired and the size of the spectral image to recover. Then the compression ratio ρ can be expressed as a linear function of the number of shots K as

$$\rho = \frac{K\left(2M\left(N + \overline{L} - 1\right)\right)}{(MNL)}, \tag{3.2}$$

Where $\overline{L}$ is the average between the number of visible and infrared bands.

In any real application, the acquired measurements are corrupted by at least a small amount of noise as sensing devices do not have infinite precision. In order to analyze the impact caused by different amounts of the sensor noise, zero-mean Gaussian noise $\boldsymbol{\omega}$ was added to the set of FPA measurements $\mathbf{g}$ as in eq. (2.7). The variance of the noise is selected such that a desired signal to noise ratio (SNR) is achieved. The SNR can be expressed as:

$$\mathrm{SNR} = 10 \log_{10}\left(\frac{\sigma_g^2}{\sigma_n^2}\right), \tag{3.3}$$

where σ_g^2 is the variance of the FPA measurement set **g,** and σ_n^2 is the variance of the noise.

4. COMPUTER SIMULATIONS AND RESULTS

Diverse simulations were performed using two hyperspectral data cubes acquired with the AVIRIS sensor [10]. The selected scenes were found in the official website of AVIRIS: Moffet and Salinas fields. Both hyperspectral images were acquired between 400 to 2500 ηm, containing 224 spectral reflectance bands. For each band on the scenes, the data was rescaled so that only 128x128 pixels are used due to the restriction of using only dyadic numbers required for the fast implementation of the 2-D wavelet transform. Furthermore, once the water absorption bands were removed, the remaining bands were linearly averaged so that the final data has 8 bands for the visible range and 8 bands for the IR.

This first data set, the Moffet field aerial view, contains 16 classes of agricultural components like corn, oats, wheat, woods, grass and so on. The original spatial resolution is 1924x753 pixels. The number of bands was reduced to 190 by removing bands covering the region of water absorption: {1328.125 ηm – 1440.625 ηm}, {1487.500 ηm – 1515.625 ηm} and {1834.375 ηm – 1984.375 ηm}. An RGB representation of this database is presented in the upper left of Fig. 6 where the eight visible spectral bands are represented with their corresponding wavelength by using false color and the remaining eight bands belonging to the IR spectrum on gray scale.

The second spectral image was acquired over “Salinas Valley”, California. The original image size in pixels is 512x217 and as in the “Moffet Field” data cube, 36 water absorption bands were discarded from the 224 original ones, but in this case the removed bands were: {400.000 ηm – 428.125 ηm}, {1393.750 ηm – 1478.125 ηm}, {1815.625 ηm – 1975 ηm} and {2462.500 ηm – 2490.625 ηm}. This scene includes vegetables, bare soils, and vineyard fields as shown in Fig. 7.

This section is divided into two subsections. In the first, the goal is to compare the sparsity of the spectral images when their visible and IR spectral band sets are separately and jointly sparsified. In the second, the analysis refers to determine the performance of the proposed system against the parallelized CASSI systems.

Figure 6. Spectral bands of "Moffet field" data cube with wavelengths ranging from 400 nm to 2275 nm.

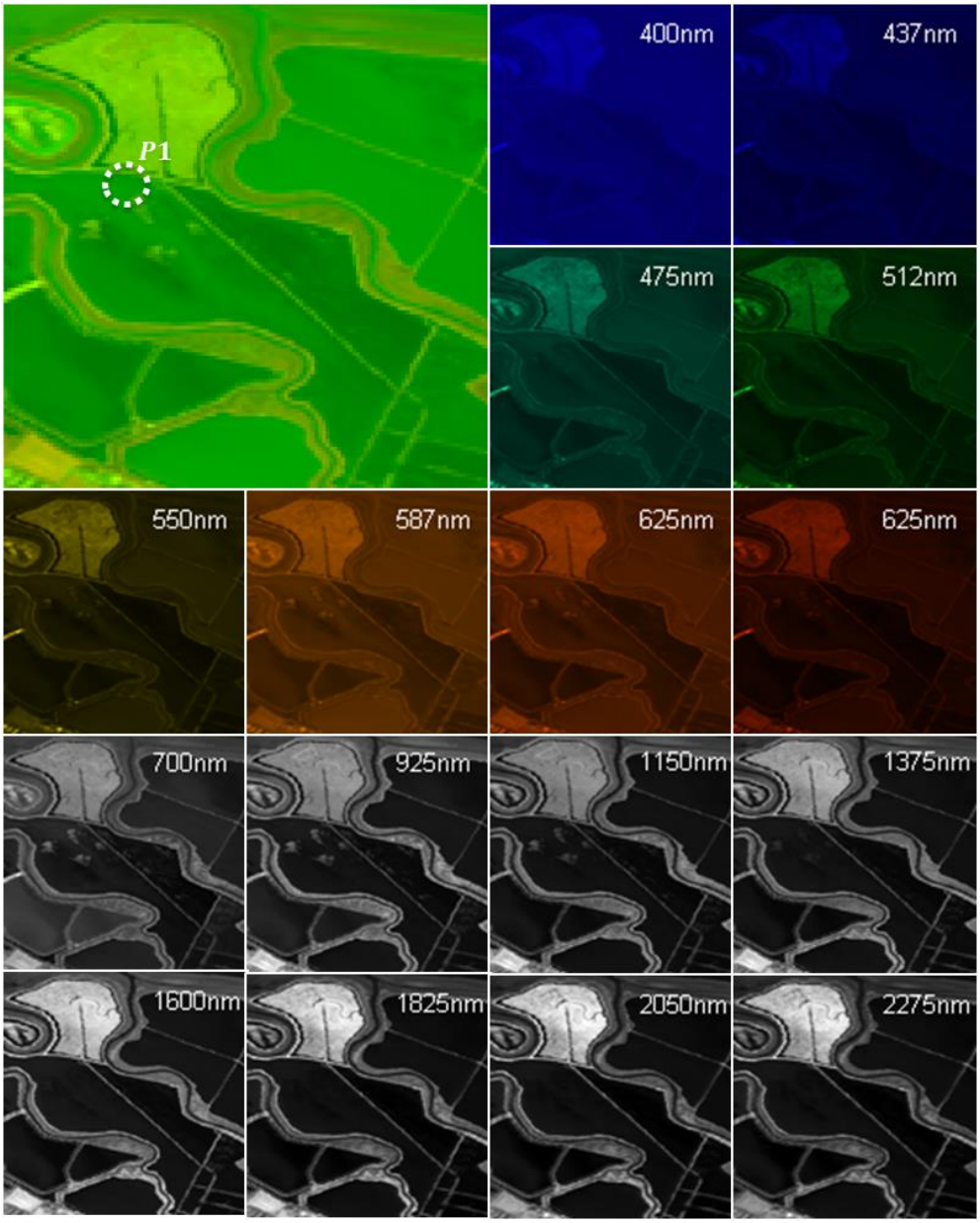

Each spectral slice has a spatial resolution of 128x128 pixels (Database 1).

Figure 7. Spectral bands of "Salinas" data cube with wavelengths ranging from 400 nm to 2275 nm.

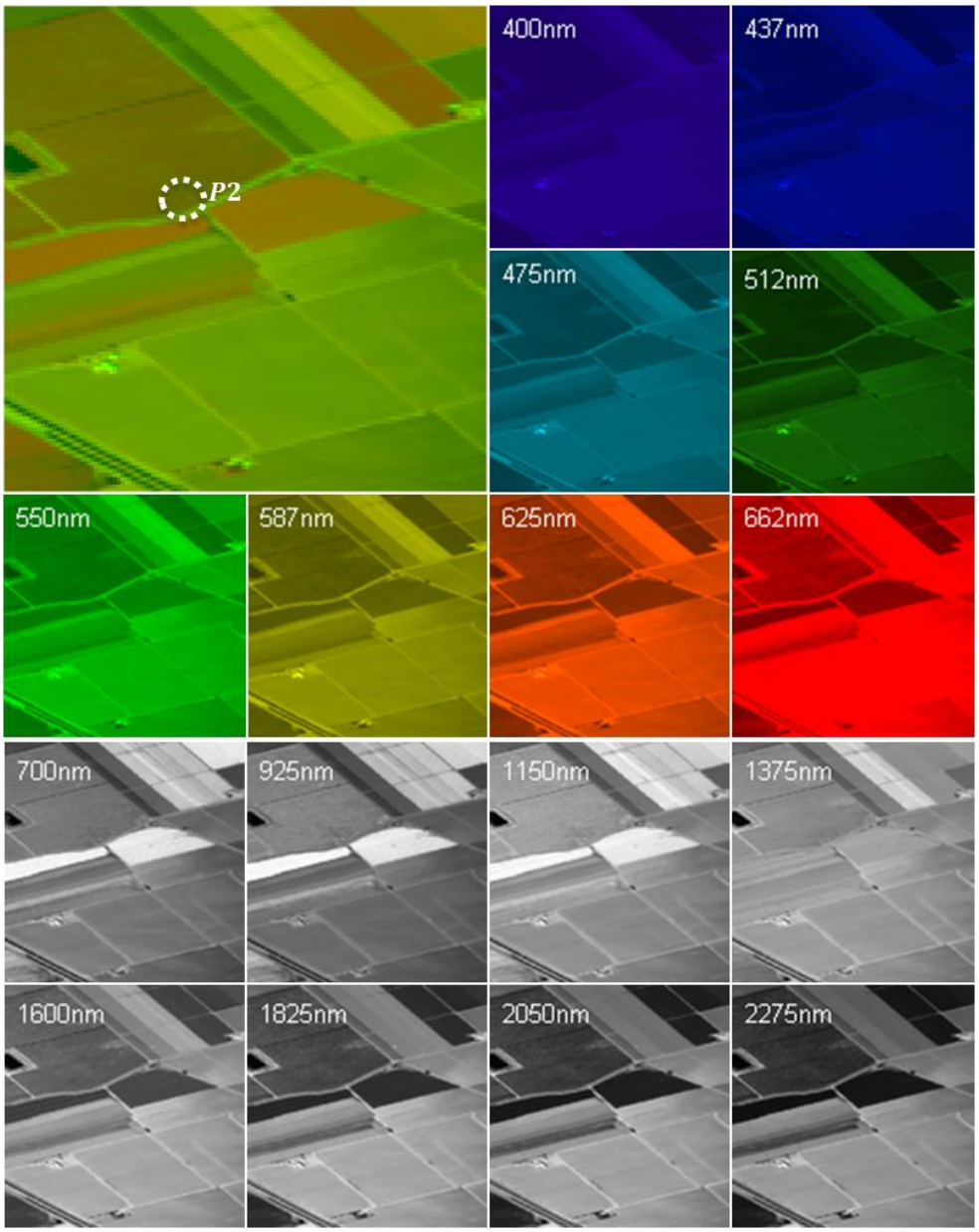

Each spectral slice has a spatial resolution of 128x128 pixels (Database 2).

4.1 POWER ANALYSIS OF THE SPARSE REPRESENTATIONS

The objective of this experiment is to know if the infrared extra content provides valuable information that increases the sparsity in the images when the whole data cube $\mathbf{f}$ is represented in the sparsifying basis $\mathbf{\Psi}_{3D}$. The energy contained in the jointly transformed $\boldsymbol{\theta} = \mathbf{\Psi}_{3\mathrm{D}}{}^{-1}\mathbf{f}$ is compared with the energy of the sorted vector of coefficients $\widehat{\boldsymbol{\theta}} = [\boldsymbol{\theta}_{\mathrm{V}}; \boldsymbol{\theta}_{\mathrm{IR}}]$, where $\boldsymbol{\theta}_{\mathrm{V}} = \mathbf{\Psi}_{3\mathrm{D}}{}^{-1}\mathbf{f}_{\mathrm{V}}$ and $\boldsymbol{\theta}_{\mathrm{IR}} = \mathbf{\Psi}_{3\mathrm{D}}{}^{-1}\mathbf{f}_{\mathrm{IR}}$ are transformed separately.

For this purpose, we compare the percentage of energy content as a function of the number of coefficients for $\boldsymbol{\theta}$ and $\widehat{\boldsymbol{\theta}}$. A zoomed version for the first 25 coefficients is shown in Fig. 8. There can be noticed that in Database 2 (Fig. 8 right), $\boldsymbol{\theta}$ has a sharper growth since more than the 80% of the energy is contained in the first 5 coefficients compared with the 60% achieved in the separated approach. Conversely, in the first Database (Fig. 8 left), $\boldsymbol{\theta}$ is less sparse compared with $\widehat{\boldsymbol{\theta}}$ since it presents a slower power growth. It is important to take into account that regardless the approach used to obtain the sparse representation, the total energy of each database must add up to the same value for both cases, and the difference lies on the energy distribution among the coefficients.

Figure 8. Comparison percentage of energy contained as a function of the number of coefficients for (a) Moffet field and (b) Salinas databases.

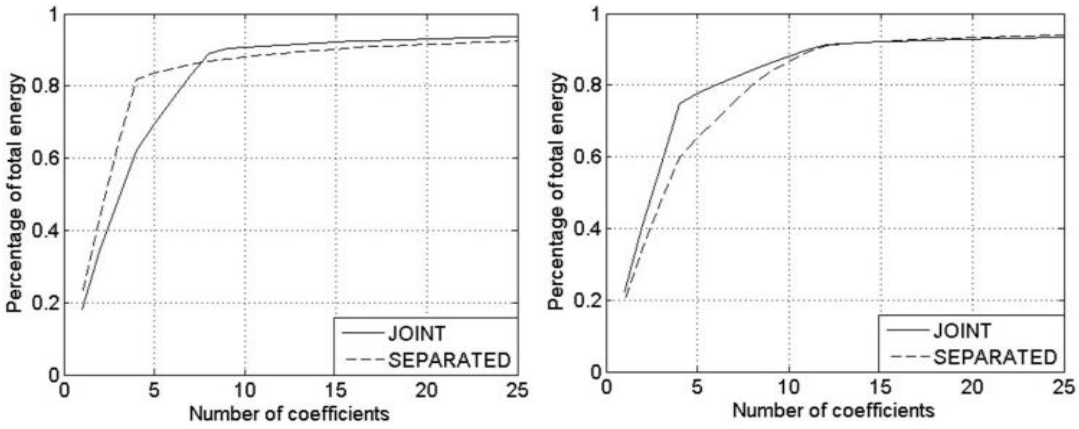

Under the assumption that the sparsity of the signal is highly related to the correlation between all the bands, a correlation analysis was done and the resulting 16x16 matrices are presented in Fig. 9. There, it can be observed that as expected, Database 2 (right) presents high correlation between all the visible bands, and these in turn with the latest infrared bands. Thus, the more correlated the bands of the data cube are, the greater is the sparsity achieved.

Figure 9. Correlation matrix for (a) Moffet field and (b) Salinas databases.

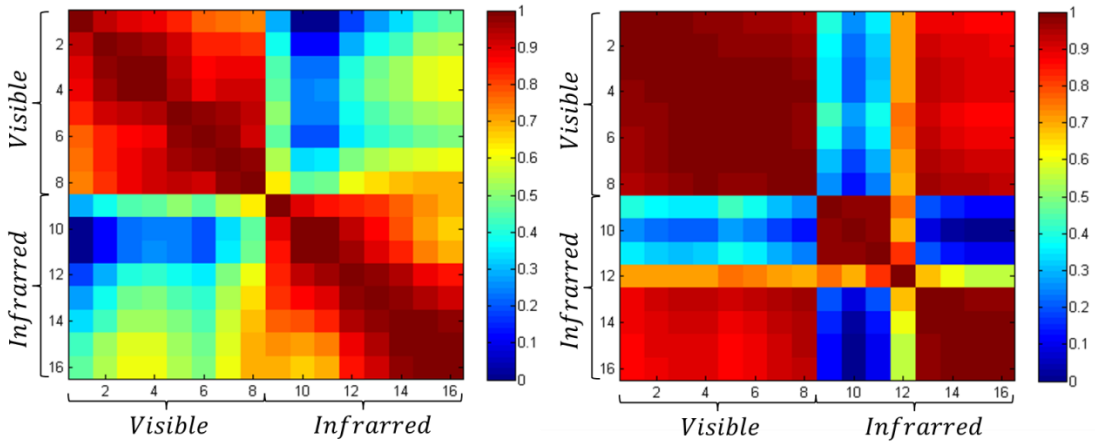

4.2 RECONSTRUCTION OF THE SPECTRAL IMAGES

Diverse simulations were performed in order to determine the best Peak-Signal-to-Noise-Ratio (PSNR) of the reconstructed data cubes as a function of the transmittance, the compression ratio and the Gaussian noise applied to the measurements. In this section, the performance of the proposed DA-CASSI system, in conjunction with the conventional CASSI is compared in the reconstruction of both databases.

To compare the performance of the DA-CASSI model with the traditional CASSI, two different analysis were proposed. The first experiment focuses on the impact of two important factors, the coded aperture transmittance ξ and the number of snapshots taken (as a function of ρ); the second refers to the noise analysis for the best results obtained in the first part. For both analysis, the regularization parameter τ has been carefully selected so that optimum results are obtained and each experiment was repeated five times for every case and the results were averaged. Finally, all simulations were conducted and timed using an Intel Core i7 3960x3.3 GHz processor with 32 GB RAM memory.

4.2.1 Optimal parameters analysis In order to analyze the effect of the transmittance, we used several values of $\xi \in \{0.3, 0.4, 0.5, 0.6, 0.7, 0.8\}$. Transmittances above 0.8 are not analyzed given that they require the solution of an extremely ill-posed inverse problem. Besides, transmittances below 0.3 are also discarded due to the extremely low light efficiency [17]. To analyze the effect of the number of snapshots, we varied *K* from 1 to 4 or equivalently the compression ratio $\rho = 13.18, 26.37, 39.55$ and 52.73%.

Figure 10 depicts the reconstruction results obtained in the transmittance analysis at a different number of snapshots for both databases using the traditional CASSI and the proposed DA-CASSI. It can be observed that for a given ξ and regardless of the database used, the reconstructed PSNR values increase as *K* increases. In addition, it can be noticed that on average, the best results were always obtained for transmittances between 0.4 and 0.7.

A more detailed comparison can be quantitatively done by analyzing Table 3, where the averaged PSNR of the reconstructed data cubes are presented as a function of the optimal transmittance value for each number of shots.

Figure 10. Impact of the transmittance ξ in the PSNR of the reconstructed images as a function of the number of snapshots K for (a) Moffet field and (b) Salinas data cubes.

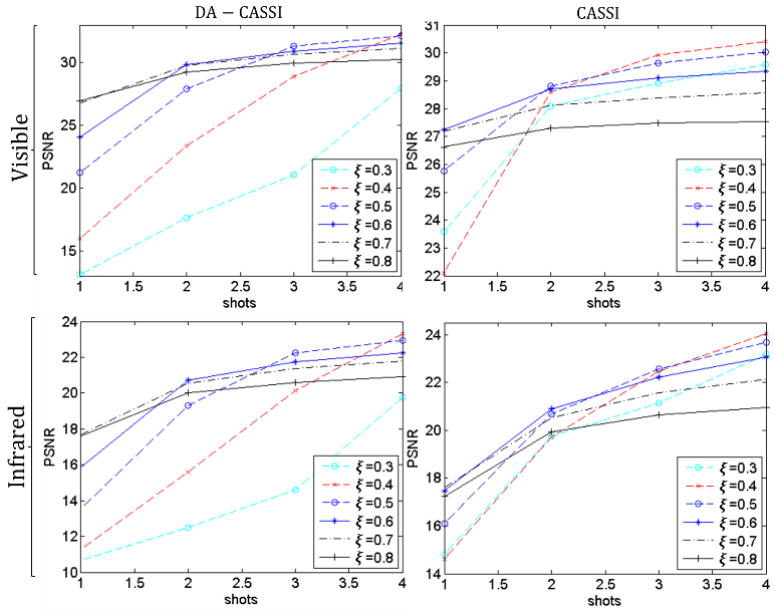

(a) Database 1. (Top-left) Visible using DA-CASSI, (Top-right) IR using DA-CASSI, (Bottom-left) Visible using CASSI (Bottom-right) IR using CASSI.

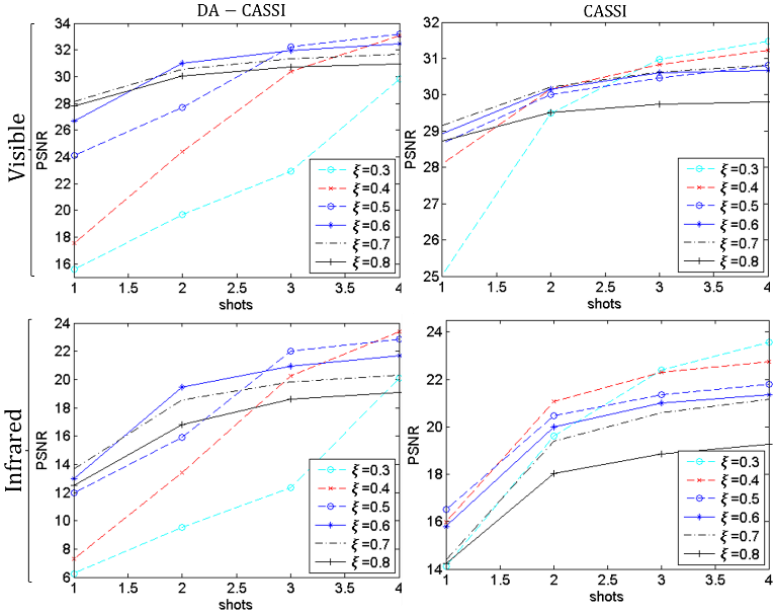

(b) Database 2. (Top-left) Visible using DA-CASSI, (Top-right) IR using DA-CASSI, (Bottom-left) Visible using CASSI (Bottom-right) IR using CASSI.

Table 3. Averaged PSNR of the reconstructed bands for the optimal transmittance values as a function of K.

Database	*K*	ρ (%)	ξ opt	DA-CASSI V [dB]	DA-CASSI IR [dB]	CASSI V [dB]	CASSI IR [dB]
No. 1	1	13,18	0.7	26,6509	17,6513	27,0959	17,5388
Moffet	2	26.37	0.6	**29,8386**	20,7392	28,7246	20,9411
128x128	3	39.55	0.5	**30.2965**	21,3615	29,6595	22,4423
x16	4	52.73	0.4	**32,2758**	23,3369	30,4906	23.9994
No. 2	1	13,18	0.7	28,0924	13,5813	29,1776	14,4470
Salinas	2	26.37	0.6	**30.3291**	18,4602	30,1501	20,2014
128x128	3	39.55	0.5	**32,2978**	**21,7665**	30,5644	21,3919
X16	4	52.73	0.4	**33,2214**	**23,6287**	31,2152	22,8143

From Table 3, it can be observed that: (i) As the two databases are the same size, the compression ratio ρ is the same for a given K and in turn, its optimal transmittance value ξ_{opt} is inversely related to the number of shots; (ii) for the visible range, the proposed DA- CASSI model recovers the bands with higher accuracy yielding to a gain of up to 2 dB when more than 2 FPA shots are used; (iii) as a consequence of the low correlation between the infrared bands, the results obtained for this range are lower than in the visible one. However, for Database 2, due to the better sparsity boosted by the high correlation presented between the visible and the last four infrared bands, the proposed system is able to surpass the traditional CASSI in up to 1 dB when more than 2 snapshots are used.

For both databases the best results are obtained for ξ=0.4 and ρ=52.73%, and the reconstructed bands with their corresponding attained PSNR are shown in Fig. 11. In summary, it is possible to asseverate that the improvement achieved in the DA-CASSI, is caused not only by the greater number of measurements used in the reconstruction per iteration compared with the CASSI system, but also by the correlation between the visible and infrared bands that boost the sparsity when this is high. Otherwise, the incoherence does not affect the performance as the sensing and sparsifying basis are the same for both models.

Figure 11. Comparison of the best achieved reconstructed images (ξ=0.4 and ρ=52.73%) between CASSI and DA-CASSI for (a) Moffet field and (b) Salinas databases.

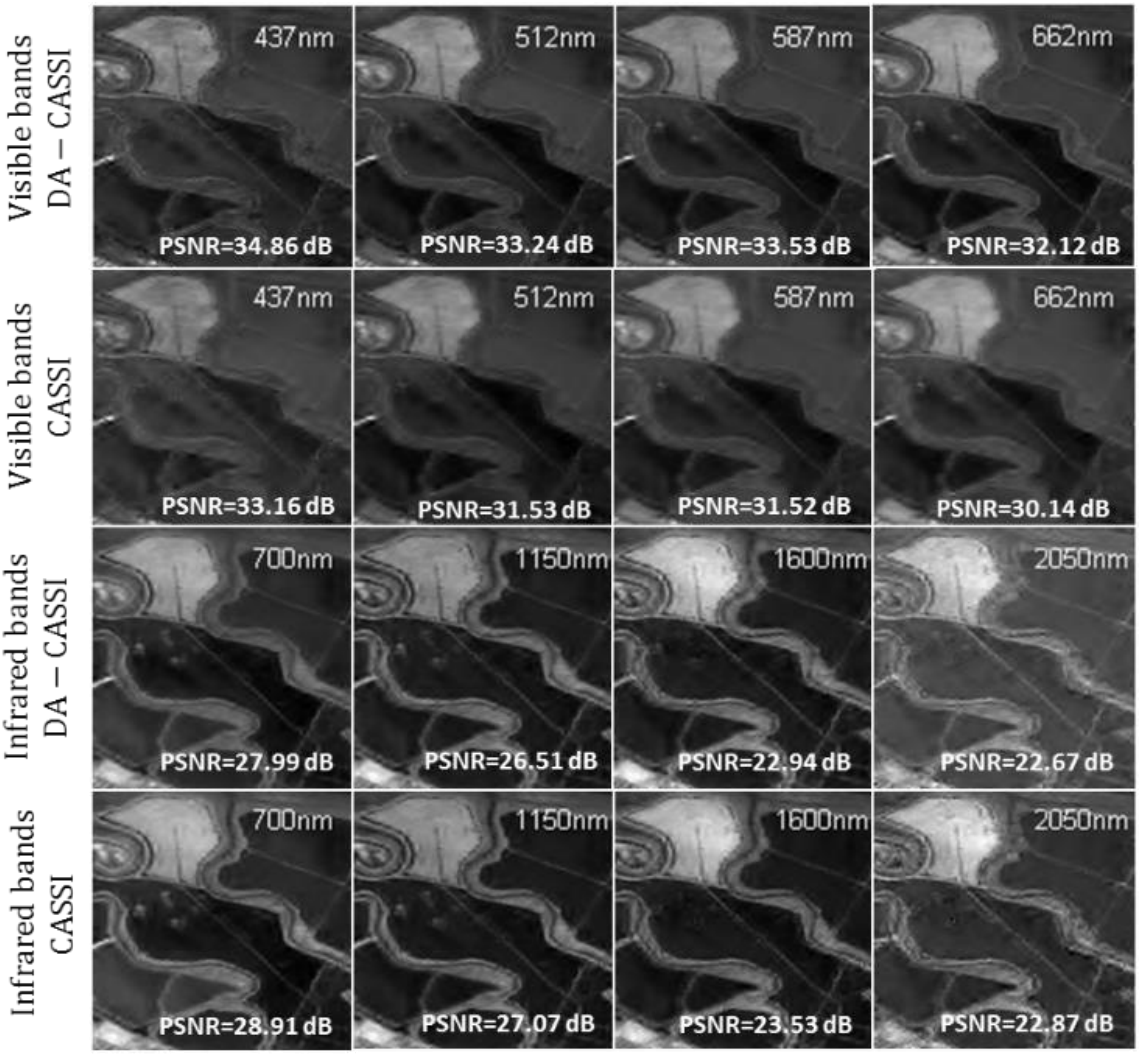

(a) Database 1. Four reconstructed bands from (first row) visible range using DA-CASSI (second row); visible range using CASSI (third row); IR range using DA-CASSI (last row) and IR range using CASSI.

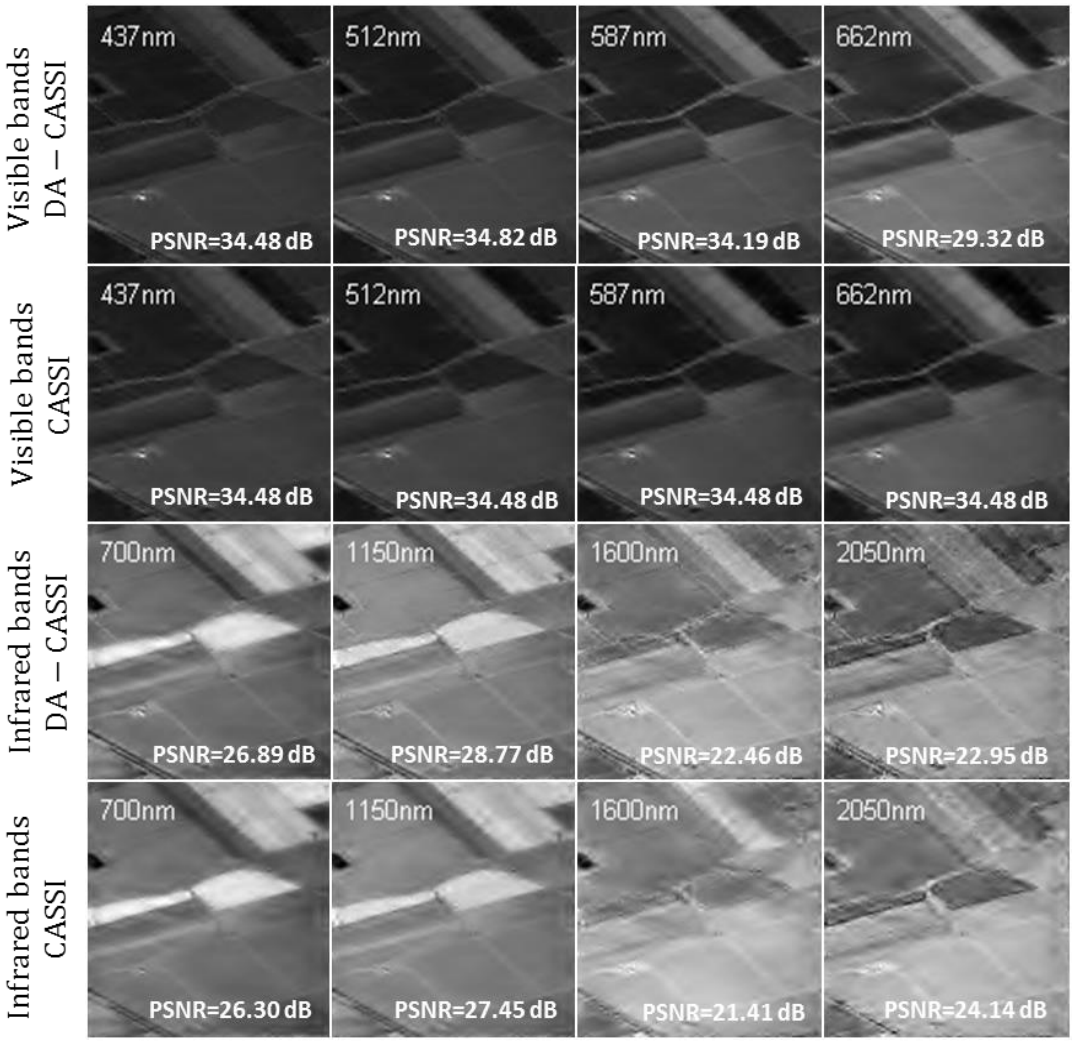

(b) Database 2. Four reconstructed bands from (first row) visible range using DA-CASSI (second row); visible range using CASSI (third row); IR range using DA-CASSI (last row) and IR range using CASSI.

In order to analyze the spectral performance, two spatial points were randomly chosen from each database (P1 and P2 in Fig. 6 and Fig. 7 respectively) and their spectral signatures are shown in Fig. 12. It can be observed that the signature reconstructed with the DA-CASSI fits better to the original curve.

Figure 12. Spectral signatures of P1 and P2 for ξ=0.4, ρ=52.73%. (a) Database 1. (b) Database 2.

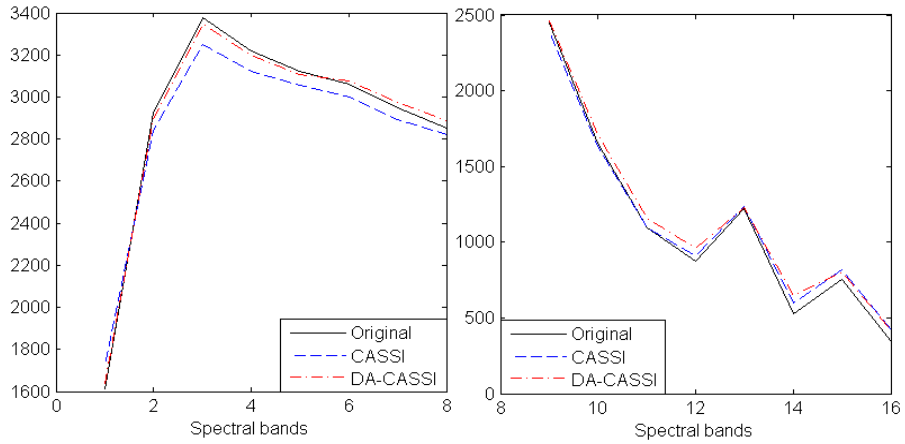

(a) Database 1. Reconstructed signatures of P1 in Fig. 6 for the: (left) Visible range and (right) Infrared range.

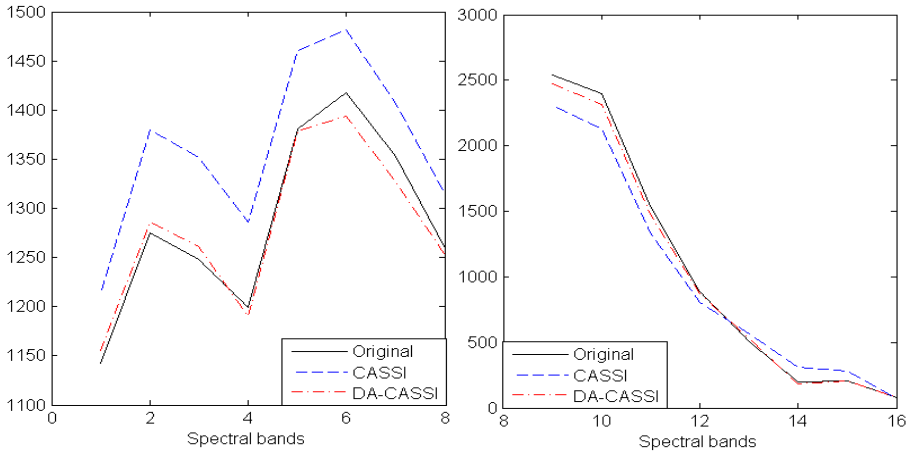

(b) Database 2. Reconstructed signatures of P2 in Fig. 7 for the: (left) Visible range and (right) Infrared range.

4.2.2 Noise analysis: We have shown that the proposed system efficiently recovers the spectral images from just a few measurements, but in order to be truly powerful, it is necessary for the DA-CASSI system to be able to deal with noise. For this reason, the best performed measurements obtained in the former analysis have been corrupted with five different amounts of noise and the results were compared. Table 4 shows the impact of the noise added to the measurements in

the PSNR of the reconstructed images, as a function of the SNR. As is shown there, the PSNR improves as the signal to noise ratio increases ranging from 10 to 40 dB.

Tabla 4 Averaged PSNR of the reconstructed bands for ξ=0.4 and ρ=52.73% as a function of the SNR noise.

Database	ρ(%)	SNR [dB]	DA-CASSI V [dB]	DA-CASSI IR [dB]	CASSI V [dB]	CASSI IR [dB]
No. 1 Moffet 128x128x16	52.73	10	28.931	17.591	29.008	20.832
		20	32.092	21.203	30.097	21.106
		30	32.204	21.556	30.321	21.423
		40	**32.249**	23.331	30.424	**23.854**
No. 2 Salinas 128x128x16	52.73	10	30.102	19.021	30.045	20.897
		20	33.064	22.989	30,984	22.331
		30	33.102	23.064	31.092	22.435
		40	**33.145**	**23.399**	31.213	22.528

Note how the reconstruction quality increases as the noise decreases. Also notice that the DA-CASSI outperforms the traditional CASSI in the visible range, even when there is noise present. Figure 13 shows the first reconstructed band of each spectral range at a fixed transmittance (ξ=0.4) and number of shots (ρ=52.73%) for SNR=10, 20, 30 and 40 dB obtained with the CASSI and the DA-CASSI model.

Fig. 13. Impact of the noise using the DA-CASSI and CASSI models when ξ=0.4, ρ=52.73% and varying SNR= 10, 20, 30 and 40 dB from left to right for (a) Moffet fields and (b) Salinas.

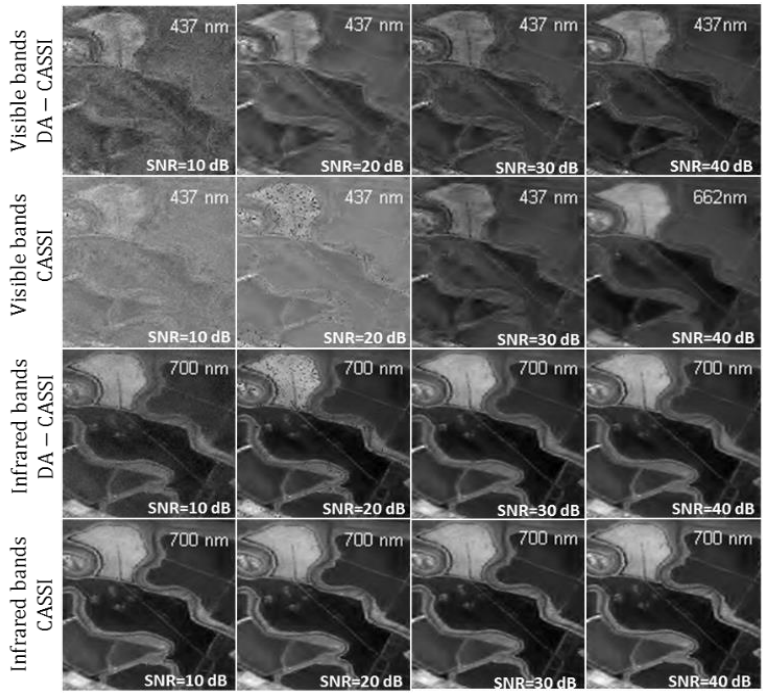

a) Database 2. Moffet fields.

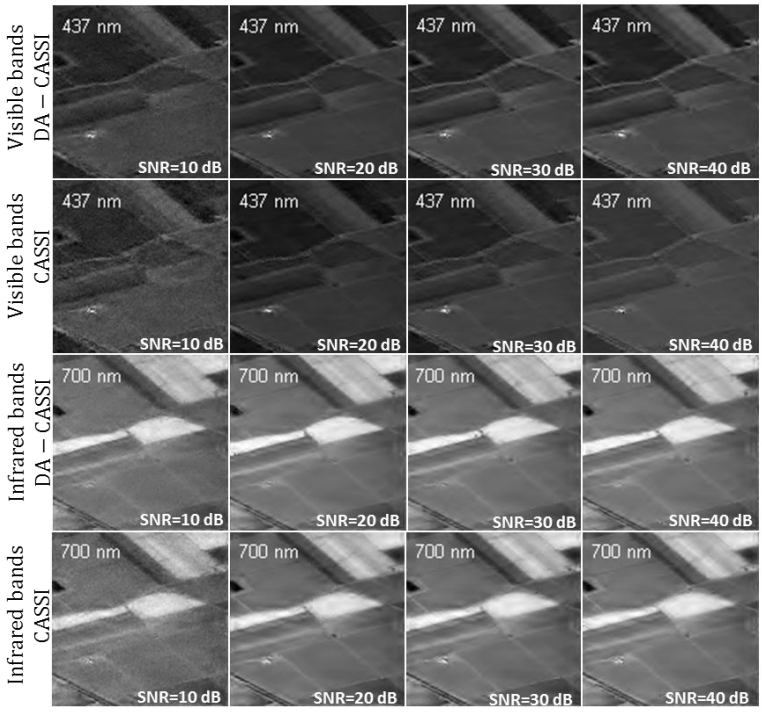

b) Database 2. Salinas.

5. CONCLUSIONS

- An optical architecture for coded-aperture based multishot spectral imaging system in the visible and near infrared range was developed. The architecture design as well as the mathematical model for the single-frame and multi-frame DA-CASSI system have been proposed as a way to accurately and simultaneously obtain the same spatial information in the visible and infrared range of the electromagnetic spectrum.

- The DA-CASSI system rises as a solution to reduce the implementation costs of such a broad spectrum acquisition system. The improvement achieved in the proposed system, is caused not only by the greater number of measurements used in the reconstruction compared with the CASSI system, but also by the correlation between the visible and infrared bands that boosts the sparsity when this is high.

- Based on the results of the reconstructed spectral images, it was proved that for a given number of snapshots *K*, the transmittance value for which the best achieved reconstructed images is obtained ξ_{opt}, is inversely related to K.

- The PSNR of the reconstructed images with the proposed model, in average reaches up to 33,22 dB and 23,63 for the visible and infrared bands respectively.

- The multi-shot approach improves the single-shot code aperture based optical system at the cost of acquiring multiple FPA measurements. To do so, the objective and the coded aperture remain static and invariant while multiple shots are being captured.

6. FUTURE WORK

- It is recommended the optical implementation of the proposed architecture since it allows higher quality reconstructed images at a reduced cost, compared to the traditional CASSI systems used in parallel.

- Include within the DA-CASSI model a way to overcome the mismatch due to the differences in spatial resolution of the visible sensitive detectors compared to the infrared detectors.

REFERENCES

[1] Arce, G. R., Brady, D. J., Carin, L., Arguello, H. and Kittle, D. S. Compressive coded aperture spectral imaging: an introduction. IEEE Signal Processing, vol. 31(1), pp. 105-115, 2014.

[2] Shaw, G.A. and Burke, H. H. K. Spectral imaging for remote sensing. Lincoln Laboratory Journal, vol. 14(1), pp. 3-28, 2003.

[3] Vorovencii, I. The Hyperspectral Sensors used in Satellite and Aerial Remote Sensing. Bulletin of the Transilvania University of Braşov, vol. 2(51), 2009.

[4] Govender, M., Chetty K. and Bulcock H. A review of hyperspectral remote sensing and its application in vegetation and water resource studies. Water Sa, vol. 33(2), 2007.

[5] Gowen, A.A., O'Donnell, C., Cullen, P. J., Downey G. and Frias J. M. Hyperspectral imaging–an emerging process analytical tool for food quality and safety control. Trends in Food Science and Technology, vol. 18(12), pp. 590-598, 2007.

[6] Cen, H. and He, Y. Theory and application of near infrared reflectance spectroscopy in determination of food quality. Trends in Food Science and Technology, vol. 18(2), pp. 72-83, 2007.

[7] Ding, H. B. and Xu, R. J. Differentiation of beef and kangaroo meat by visible/near-infrared reflectance spectroscopy. Journal of Food Science, vol. 64(5), pp. 814-817, 1999.

[8] Pfitzner, K., Martin, P. and Bayliss, P. Compact Airborne Spectrographic Imager (CASI) and ground-based spectrometer data of Nabarlek an. 2004.

[9] Gat, N. Imaging spectroscopy using tunable filters: a review. Proceedings of SPIE, pp. 50-64, 2000.

[10] GREEN, R. O., EASTWOOD, M. L., SARTURE, C. M., CHRIEN, T. G., ARONSSON, M., CHIPPENDALE, B. J. and WILLIAMS, O. Imaging spectroscopy and the airborne visible/infrared imaging spectrometer (AVIRIS). Remote Sensing of Environment, vol. 65(3), pp. 227-248, 1998.

[11] Candès, E. J. and Wakin, M. B. An introduction to compressive sampling. IEEE Signal Processing Magazine, vol. 25(2), pp. 21-30, 2008.

[12] Ye, P. Arguello, H. and Arce, G. R. Spectral aperture code design for multi-shot compressive spectral imaging, In Digital Holography and Three-Dimensional Imaging (OSA), p. DWA6, 2010.

[13] Holzwarth, S., Müller, A., Habermeyer, M., Richter, R., Hausold, A., Thiemann, S. and Strohl, P. HySens-DAIS 7915/ROSIS imaging spectrometers at DLR. In Proceedings of the 3rd Earsel Workshop on Imaging Spectroscopy, Herrsching, Germany, pp. 3-14, 2003.

[14] Pearlman, J. S., Barry, P. S., Segal, C. C., Shepanski, J., Beiso, D. and Carman, S. L. Hyperion, a space-based imaging spectrometer. Geoscience and Remote Sensing, IEEE Transactions on, vol. 41(6), pp. 1160-1173, 2003.

[15] Duarte, M. F. and Baraniuk, R. G. Kronecker compressive sensing. IEEE Transactions on Image Processing, vol. 21(2), pp. 494-504, 2012.

[16] Arguello, H. and Arce, G. R. Code aperture optimization for spectrally agile compressive imaging. Journal of the Optical Society of America, vol. 28(11), pp. 2400-2413, 2011.

[17] Rueda, H., Arguello, H. and Arce, G. R. DMD-based implementation of patterned optical filter arrays for compressive spectral imaging. Journal of the Optical Society of America, vol. 32(1), pp. 80-89, 2015.

[18] Kittle, D., Choi, K., Wagadarikar, A. and Brady, D. J. Multiframe image estimation for coded aperture snapshot spectral imagers. Applied Optics, vol. 49(36), pp. 6824-6833, 2010.

[19] Wu, Y., Mirza, I. O., Arce, G. R. and Prather, D. W. Development of a digital-micromirror-device-based multishot snapshot spectral imaging system. Optics Letters, vol. 36(14), pp. 2692-2694, 2011.

[20] Figueiredo, M., Nowak, R. D. and Wright, S. J. Gradient projection for sparse reconstruction: Application to compressed sensing and other inverse problems. Selected Topics in Signal Processing, IEEE Journal of, 2007, vol. 1(4), pp. 586-597, 2007.

[21] Rueda, H., Calderon, A. R. and Arguello, H. Spectral selectivity in compressive spectral imaging based on grayscale coded apertures. Image Signal Processing and Artificial Vision (STSIVA), pp. 1-5, 2013.

BIBLIOGRAPHY

ARCE, G. R., BRADY, D. J., CARIN, L., ARGUELLO, H. and KITTLE, D. S. Compressive coded aperture spectral imaging: an introduction. IEEE Signal Processing, vol. 31(1), pp. 105-115, 2014.

ARGUELLO, H. and ARCE, G. R. Code aperture optimization for spectrally agile compressive imaging. Journal of the Optical Society of America, vol. 28(11), pp. 2400-2413, 2011.

CANDÈS, E. J. and WAKIN, M. B. An introduction to compressive sampling. IEEE Signal Processing Magazine, vol. 25(2), pp. 21-30, 2008.

CEN, H. and HE, Y. Theory and application of near infrared reflectance spectroscopy in determination of food quality. Trends in Food Science and Technology, vol. 18(2), pp. 72-83, 2007.

DING, H. B. and XU, R. J. Differentiation of beef and kangaroo meat by visible/near-infrared reflectance spectroscopy. Journal of Food Science, vol. 64(5), pp. 814-817, 1999.

DUARTE, M. F. and BARANIUK, R. G. Kronecker compressive sensing. IEEE Transactions on Image Processing, vol. 21(2), pp. 494-504, 2012.

FIGUEIREDO, M., NOWAK, R. D. and WRIGHT, S. J. Gradient projection for sparse reconstruction: Application to compressed sensing and other inverse problems. Selected Topics in Signal Processing, IEEE Journal of, 2007, vol. 1(4), pp. 586-597, 2007.

GAT, N. Imaging spectroscopy using tunable filters: a review. Proceedings of SPIE, pp. 50-64, 2000.

GOVENDER, M., CHETTY K. and BULCOCK H. A review of hyperspectral remote sensing and its application in vegetation and water resource studies. Water Sa, vol. 33(2), 2007.

GOWEN, A.A., O'DONNELL, C., CULLEN, P. J., DOWNEY G. and FRIAS J. M. Hyperspectral imaging–an emerging process analytical tool for food quality and safety control. Trends in Food Science and Technology, vol. 18(12), pp. 590-598, 2007.

GREEN, R. O., EASTWOOD, M. L., SARTURE, C. M., CHRIEN, T. G., ARONSSON, M., CHIPPENDALE, B. J. and WILLIAMS, O. Imaging spectroscopy and the airborne visible/infrared imaging spectrometer (AVIRIS). Remote Sensing of Environment, vol. 65(3), pp. 227-248, 1998.

HOLZWARTH, S., MÜLLER, A., HABERMEYER, M., RICHTER, R., HAUSOLD, A., THIEMANN, S. and STROHL, P. HySens-DAIS 7915/ROSIS imaging spectrometers at DLR. In Proceedings of the 3rd Earsel Workshop on Imaging Spectroscopy, Herrsching, Germany, pp. 3-14, 2003.

KITTLE, D., CHOI, K., WAGADARIKAR, A. and BRADY, D. J. Multiframe image estimation for coded aperture snapshot spectral imagers. Applied Optics, vol. 49(36), pp. 6824-6833, 2010.

PEARLMAN, J. S., BARRY, P. S., SEGAL, C. C., SHEPANSKI, J., BEISO, D. and CARMAN, S. L. Hyperion, a space-based imaging spectrometer. Geoscience and Remote Sensing, IEEE Transactions on, vol. 41(6), pp. 1160-1173, 2003.

PFITZNER, K., MARTIN, P. and BAYLISS, P. Compact Airborne Spectrographic Imager (CASI) and ground-based spectrometer data of Nabarlek an. 2004.

RUEDA, H., ARGUELLO, H. and ARCE, G. R. DMD-based implementation of patterned optical filter arrays for compressive spectral imaging. Journal of the Optical Society of America, vol. 32(1), pp. 80-89, 2015.

RUEDA, H., CALDERON, A. R. and ARGUELLO, H. Spectral selectivity in compressive spectral imaging based on grayscale coded apertures. Image Signal Processing and Artificial Vision (STSIVA), pp. 1-5, 2013.

SHAW, G.A. and BURKE, H. H. K. Spectral imaging for remote sensing. Lincoln Laboratory Journal, vol. 14(1), pp. 3-28, 2003.

VOROVENCII, I. The Hyperspectral Sensors used in Satellite and Aerial Remote Sensing. Bulletin of the Transilvania University of Braşov, vol. 2(51), 2009.

WU, Y., MIRZA, I. O., ARCE, G. R. and Prather, D. W. Development of a digital-micromirror-device-based multishot snapshot spectral imaging system. Optics Letters, vol. 36(14), pp. 2692-2694, 2011.

YE, P. ARGUELLO, H. and ARCE, G. R. Spectral aperture code design for multi-shot compressive spectral imaging, In Digital Holography and Three-Dimensional Imaging (OSA), p. DWA6, 2010.